MNRAS 000, 1–15 (2017) Preprint May 17, 2018 Compiled using MNRAS LATEX style file v3.0

Weak Lensing Peaks in Simulated Light-Cones: Investigating the Coupling between Dark Matter and Dark Energy

Carlo Giocoli[1,2,3]★, Lauro Moscardini[1,2,3], Marco Baldi[1,2,3], Massimo Meneghetti[2,1,3], Robert B. Metcalf[1,2]

[1] *Dipartimento di Fisica e Astronomia, Alma Mater Studiorum Università di Bologna, via Gobetti 93/2, 40129 Bologna, Italy*
[2] *INAF-OAS Osservatorio di Astrofisica e Scienza dello Spazio di Bologna, via Gobetti 93/3, 40129, Bologna, Italy*
[3] *INFN - Sezione di Bologna, viale Berti Pichat 6/2, 40127, Bologna, Italy*

May 17, 2018

ABSTRACT

In this paper, we study the statistical properties of weak lensing peaks in light-cones generated from cosmological simulations. In order to assess the prospects of such observable as a cosmological probe, we consider simulations that include interacting Dark Energy (hereafter DE) models with coupling term between DE and Dark Matter. Cosmological models that produce a larger population of massive clusters have more numerous high signal-to-noise peaks; among models with comparable numbers of clusters those with more concentrated haloes produce more peaks. The most extreme model under investigation shows a difference in peak counts of about 20% with respect to the reference ΛCDM model. We find that peak statistics can be used to distinguish a coupling DE model from a reference one with the same power spectrum normalisation. The differences in the expansion history and the growth rate of structure formation are reflected in their halo counts, non-linear scale features and, through them, in the properties of the lensing peaks. For a source redshift distribution consistent with the expectations of future space-based wide field surveys, we find that typically seventy percent of the cluster population contributes to weak-lensing peaks with signal-to-noise ratios larger than two, and that the fraction of clusters in peaks approaches one-hundred percent for haloes with redshift $z \leq 0.5$. Our analysis demonstrates that peak statistics are an important tool for disentangling DE models by accurately tracing the structure formation processes as a function of the cosmic time.

Key words: galaxies: halos - cosmology: theory - dark matter - methods: analytic - gravitational lensing: weak

1 INTRODUCTION

In the standard cosmological model, most of the energy in the Universe, approximately 70%, is in an unknown form, termed Dark Energy (hereafter DE) which has a negative pressure. This component is responsible for the late time accelerated expansion as measured by many observations (Perlmutter et al. 1999; Riess et al. 1998, 2004, 2007; Schrabback et al. 2010; Betoule et al. 2014). About 25% of the energy content is in a different unknown component termed Dark Matter (DM), whose presence has been mainly inferred from its gravitational effects given that it seems not to emit nor absorb detectable levels of radiation (Zwicky 1937; Rubin et al. 1980; Bosma 1981a,b; Rubin et al. 1985).

Following the standard scenario, cosmic structures form as a consequence of gravitational instability. Dark matter overdensities contract and build up into so-called dark matter haloes (White & Rees 1978; White & Silk 1979). Small systems collapse first when the universe is denser and then merge together to form more massive objects (Tormen 1998; Lacey & Cole 1993, 1994). Galaxy clusters sit at the top of this hierarchy as the latest nonlinear structures to form in our Universe (Kauffmann & White 1993; Springel et al.

★ E-mail:carlo.giocoli@unibo.it

2001b, 2005; Wechsler et al. 2002; van den Bosch 2002; Wechsler et al. 2006; Giocoli et al. 2007).

The large amount of dark matter present in virialized systems and within the filamentary structure of our Universe is able to bend the light emitted by background objects (Bartelmann & Schneider 2001). Because of this, the intrinsic shapes of background galaxies appear to us weakly distorted by gravitational lensing. Since lensing is sensitive to the total mass of objects and independent of how the mass is divided into the light and dark components of galaxies, groups and clusters, it represents a direct and clean tool for probing the distribution and evolution of structures in the Universe.

When light bundles emitted from background objects travel through high density regions like the centres of galaxies and clusters, the gravitational lensing effect is strong (SL): background images appear strongly distorted into gravitational arcs or divided into multiple images (Postman et al. 2012; Hoekstra et al. 2013; Meneghetti et al. 2013; Limousin et al. 2016). On the other hand, when light bundles transit the periphery of galaxies or clusters, background images are only slightly distorted and the gravitational lensing effect is termed weak (WL) (Amara et al. 2012; Radovich et al. 2015). In this way weak gravitational lensing represents an important tool for studying the matter density distributed within large scale structures. A large range of source redshifts allows one to tomographically probe the dark energy evolution through the cosmic growth rate as a function of redshift (Kitching et al. 2014; Köhlinger et al. 2016) (for a review see Kilbinger 2014). Great efforts and impressive results have been reached by weak lensing collaborations like CFHTLens (Fu et al. 2008; Benjamin et al. 2013) and KiDS (Hildebrandt et al. 2017). Some tensions may still exist between these measurements and the ones coming from the Cosmic Microwave Background (Planck Collaboration et al. 2016). Hopefully, wide field surveys from space will help to fill the gap between low- and high-redshift cosmological studies and shed more light onto the dark components of our Universe.

Gravitational lensing will be the primary cosmological probe in several experiments that will start in the near future, like LSST (LSST Science Collaboration et al. 2009) and the ESA space mission Euclid[1] (Laureijs et al. 2011). Recently, the Kilo Degree Survey (KiDS) collaboration presented a series of papers devoted to the shear peak analysis of ~ 450 deg^2 of data (Hildebrandt et al. 2017). They emphasised that peak statistics are a complementary probe to cosmic shear analysis which may break the degeneracy between the matter density parameter, Ω_m, and σ_8, the power spectrum amplitude expressed in term of the root-mean-square of the linear density fluctuation smoothed on a scale of 8 Mpc/h. In particular, Shan et al. (2017) analyzed the convergence maps reconstructed from shear catalogues using the non-linear Kaiser & Squires (1993) inversion (Seitz & Schneider 1995). They showed that, given their source redshift distribution, peaks with signal-to-noise larger than three are mainly due to systems with masses larger than $10^{14} M_\odot/h$. However, the source distribution in the KiDS observations corresponds to a galaxy number density of only 7.5 gal. per square arcmin at a median redshift of $z = 0.6$. This low number density of galaxies prevented them from performing a tomographic analysis. Within the same collaboration, by using reconstructed maps from simulations, Martinet et al. (2017) confirmed the importance of combining peak and cosmic shear analyses. In particular they pointed out that cosmological constraints in the Ω_m-σ_8 plane coming from low signal-to-noise peaks are tighter than those coming from the high-significance ones.

The strength of peak statistics in disentangling cosmological models has been discussed in the last years by several authors. In particular Maturi et al. (2011) have inspected the effect of primordial non-Gaussianity, which impacts the chance of projected large scale structures varying the peak counts. Pires et al. (2012) demonstrated that peak counts are the best statistic to break the σ_8-Ω_m degeneracy among the second-order weak lensing statistics. Reischke et al. (2016) have suggested that the extreme value statistic of peak counts can tighten even more the constraints on cosmological parameters.

In this work we will study weak lensing peak statistics in a sample of non-standard cosmological models which are characterised by a coupling term between dark energy and dark matter. We will discuss the complementarity of peak statistics with respect to cosmic shear and examine the information on non-linear scales from high significance peaks. We will discuss also the importance of tomographic analysis of peak statistics as tracers of the growth and the expansion history of the universe.

The paper is organised as follows: in Section 2 we present the numerical simulations analysed and introduce how weak lensing peaks have been identified. Statistical properties of peaks are reviewed in Section 3, while the connection between galaxy clusters and peaks is discussed in Section 4. We conclude and summarise in Section 5.

2 METHODS AND NUMERICAL SIMULATIONS

2.1 Numerical Simulations of Dark Energy Models

In this work we use the numerical simulation dataset presented by (Baldi 2012b) and partially publicly available at this url: http://www.marcobaldi.it/web/CoDECS_summary.html. The simulations have been run with a version of the widely used N-body code GADGET (Springel 2005) modified by Baldi et al. (2010), which self-consistently includes all the effects associated with the interaction between a DE scalar field and CDM particles. The CoDECS suite includes several different possible combinations of the DE field potential – the exponential (Lucchin & Matarrese 1985; Wetterich 1988) or the SUGRA (Brax & Martin 1999) potentials for example – and of the coupling function which can be either constant or exponential in the scalar field (see e.g. Baldi et al. 2011). For more details on the models we refer to Baldi (2012b).

In particular we use some simulations of the L – CoDECS sample (ΛCDM, EXP003, EXP008e3 and SUGRA003) plus ΛCDM – HS8 that is a ΛCDM simulation

[1] https://www.euclid-ec.org

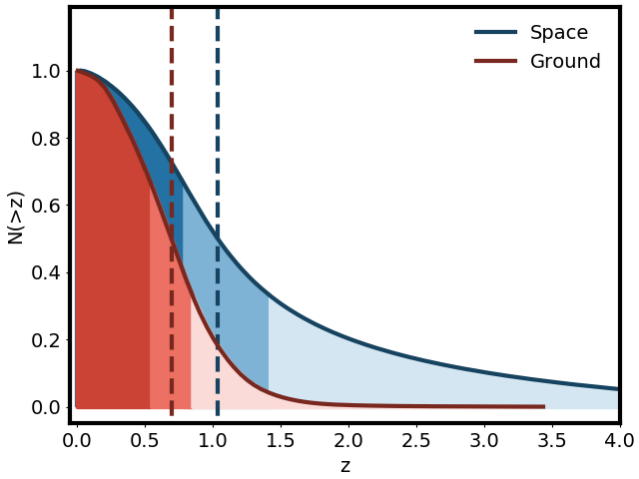

Figure 1. Cumulative normalised probability functions for two source redshift distributions, termed Space and Ground. While the Ground distribution has been build to match the source redshift distribution of CFHTLens (Kilbinger et al. 2013), the Space one corresponds to the distribution adopted by Boldrin et al. (2012, 2016) as expected from a wide field survey from space, like Euclid. The two dotted lines mark the median source redshifts in the two cases, while the different coloured regions below the curves indicate the redshift ranges in which one third of the galaxies are expected.

with the same cosmological parameters as ΛCDM but with a value of σ_8 equal to the one of EXP003. The ΛCDM – HS8 simulation has been run in order to study how the effect of the coupling between DE and DM can be disentangled from a pure Cosmological Constant model with the same power spectrum normalisation. A summary of the considered simulations with their individual model parameters is given in Table 1

We also use the information about the halo catalogue computed for each simulation snapshot using a Fried-of-Friend (FoF) algorithm with linking parameter $b = 0.2$ times the mean inter-particle separation. At each simulation snapshot, within each FoF group we also identify gravitationally bound substructures using the SUBFIND algorithm (Springel et al. 2001b). SUBFIND searches for overdense regions within a FoF group using a local SPH density estimate, identifying substructure candidates as regions bounded by an isodensity surface that crosses a saddle point of the density field, and testing that these possible substructures are physically bound with an iterative unbinding procedure. For both FoF and SUBFIND catalogues we select and store systems with more than 20 particles, and define their centres as the position of the particle with the minimum gravitational potential. It is worth noting that while the subhaloes have a well-defined mass that is the sum of the mass of all particles belonging to them, different mass definitions are associated with the FoF groups. We define as $M_{\rm FoF}$ the sum of the masses of all particles belonging to the FoF group and as M_{200} the mass around the FoF centre enclosing a density that is 200 times the critical density of the universe at the corresponding redshift.

To compare the expected results for surveys from ground and space, we adopt in our analyses two different distribution functions of sources, shown in Fig. 1. The red (blue) curve, normalised to unity, mimics the probability distribution of sources as (expected to be) observed from ground (space) photometric survey. In particular the red curve corresponds to the redshift distribution from CFHTLens (Kilbinger et al. 2013), while the blue curve corresponds to the distribution adopted by Boldrin et al. (2012, 2016). The latter has been obtained using a simulated observation with the SKYLENS code (Meneghetti et al. 2008; Bellagamba et al. 2012; Rasia et al. 2012) and identifying with SEXTRACTOR (Bertin & Arnouts 1996) sources 3 times above the background rms. The two dashed vertical lines, red and blue, mark the median redshift from ground and space, respectively. The regions shaded in three gradations of colour enclose the redshift ranges where we have one-third of the number density of sources for the two corresponding distributions. As can be seen, the source distribution from space moves toward higher redshifts with a considerable tail that extends beyond $z = 2$: the expectations from space-based observations suggest a gain of at least a factor of two in the number of galaxies per square arcmin with measurable shapes. We reasonably assume a total number density of 18 and 33 galaxies per arcmin^2 for a ground and space experiment, respectively.

2.2 Light-Cone Reconstruction and Peak Detection

We perform our weak lensing peak detection using convergence maps for different source redshifts and for various cosmological models. We employ the MAPSIM routine developed by Giocoli et al. (2015) to construct 25 independent light-cones from the snapshots of our numerical simulations. We build the lens planes from the snapshots while randomising the particle positions by changing sign of the comoving coordinate system or arbitrarily selecting one of the nine faces of the simulation box to be located along the line-of-sight. If the light-cone reaches the border of a simulation box before it has reached a redshift range where the next snapshot will be used, the box is re-randomised and the light-cone extended through it again. The lensing planes are built by mapping the particle positions to the nearest pre-determined plane, maintaining angular positions, and then pixelizing the surface density using the triangular-shaped cloud method. The selected size of the field of view is 5×5 sq. degrees and the maps are resolved with 2048×2048 pixels, which corresponds to a pixel resolution of about 8.8 arcsec. Through the lens planes we produce the corresponding convergence maps for the desired source redshifts using the GLAMER code (Metcalf & Petkova 2014; Petkova et al. 2014; Giocoli et al. 2016).

As done by Harnois-Déraps & van Waerbeke (2015b), for the lens planes stacked into the light-cones we define the *natural* source redshifts as those lying at the end of each constructed lens planes. By construction our light-cone has the shape of a pyramid where the observer is located at the vertex and the base extends up to the maximum redshift chosen to be $z = 4$.

In wide field weak lensing analysis it is worth mentioning that intrinsic alignments (IAs) of galaxies may bias the weak lensing signal. However Shan et al. (2017) have shown that considering an Intrinsic Alignment (IA hereafter) am-

Table 1. The list of the cosmological models considered in the present work and their specific parameters. All the models have the same amplitude of scalar perturbations at $z_{\rm CMB} \approx 1100$, but have different values of σ_8 at $z = 0$. In short, α is a parameter describing the slope of the scalar field potential, $\beta(\phi)$ is the coupling function describing the rate of energy-momentum exchange with dark matter, and $w_\phi(z = 0)$ is the effective equation of state parameter (p/ρ). See Baldi (2012b) for details.

Model	Potential	α	$\beta(\phi)$	$w_\phi(z = 0)$	$\sigma_8(z = 0)$
ΛCDM	$V(\phi) = A$	–	–	−1.0	0.809
ΛCDM – HS8	$V(\phi) = A$	–	–	−1.0	0.967
EXP003	$V(\phi) = Ae^{-\alpha\phi}$	0.08	0.15	−0.992	0.967
EXP008e3	$V(\phi) = Ae^{-\alpha\phi}$	0.08	$0.4\exp[3\phi]$	−0.982	0.895
SUGRA003	$V(\phi) = A\phi^{-\alpha}e^{\phi^2/2}$	2.15	−0.15	−0.901	0.806

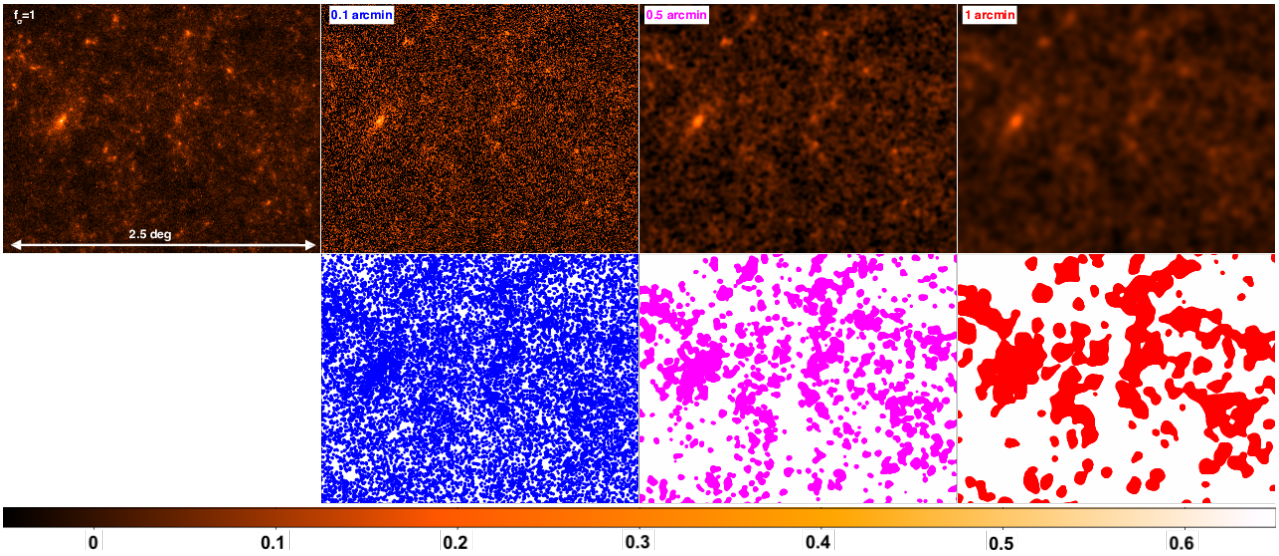

Figure 2. Noised and smoothed convergence maps considering different choices for the filter θ_F. The top left panel shows the original convergence map. The other top panels, moving from left to right, display the convergence maps artificially noised and filtered considering θ_F 0.1, 0.5 and 1 arcmin. The bottom sub-panels display the regions, in the corresponding maps, above the noise level.

plitude as computed from the cosmic shear constraints by Hildebrandt et al. (2017), the relative contribution of IA to the noise variance of the convergence is very small and well bellow 0.6% with respect to randomly oriented intrinsic ellipticities. Thus, to first approximation, we assume that the galaxies are intrinsically randomly oriented.

Noise can affect cosmological lensing measurements and results in possible biased constraints on cosmological parameters. One of the methods used to suppress the noise in reconstructed weak lensing fields is smoothing. Since weak gravitational lensing is by definition a weak effect, it is necessary to average over a sufficient number of source galaxies in order to obtain a measurement. Because of the central limit theorem, after smoothing the statistical properties of the noise field are expected to be close to a Gaussian distribution. For the noise and the characterisation of the convergence maps we follow the works of Lin & Kilbinger (2015a,b). The convergence maps $\kappa(x, y)$ that we produce from our ray-tracing procedure are only characterised by the discreteness of the density field sampled with collisionless particles: the so-called particle noise. However, to mimic the presence of galaxy shape noise, from which the convergence map is inferred from real observational data, we add to $\kappa(x, y)$ a noise field $n(x, y)$ that accounts for this. If we assume that the intrinsic ellipticities of the source galaxies are uncorrelated we can describe $n(x, y)$ as a Gaussian random field with variance:

$$\sigma^2_{\rm noise} = \frac{\sigma^2_\epsilon}{2}\frac{1}{2\pi\theta^2_F n_g}\,, \tag{1}$$

where $\sigma_\epsilon = 0.25$ is the rms of the intrinsic ellipticity of the sources, n_g the galaxy number density and θ_F represents the smoothing scale of a Gaussian window function filter, that we apply to the noised convergence map to suppress the pixel noise (Lin & Kilbinger 2015a; Zorrilla Matilla et al. 2016; Shan et al. 2017). We indicate with $k_{n,F}$ the noised and filtered convergence map. Consistent with the choice made by other authors we adopt a scale of 1 arcmin for the smoothing scale which represents the optimal size to isolate the contribution of massive haloes typically hosting galaxy clusters. For descriptive purposes, in the top left panel of Figure 2 we display the convergence map with an aperture of 2.5 deg on a side and $z_s = 1.12$. In the three panels on the left the noise has been added and the map has been smoothed assuming different choices of θ_F, 0.1, 0.5 and 1 arcminutes, from left to right, respectively. The coloured regions in the bottom panels mark the pixels in the image above that are above the noise level $f_\sigma = 1$ with:

$$f_\sigma = \frac{\kappa_{n,F}}{\sigma_{\rm noise}}\,. \tag{2}$$

From the figure we can see that peaks identified in the convergence fields with small values of θ_F are dominated by false detections caused by the noise level. For larger θ_F values the peak locations consistently follow the locations of the interposed halos within the field-of-view.

In our analysis we consider two natural source redshifts corresponding to $z_s = 0.75$ and $z_s = 1.12$ that are the medians of the two source redshift distributions as displayed in Fig. 1 [2]. The top panels of Fig. 3 displays the convergence maps of a light-cone realisation from the ΛCDM simulation considering these two source redshifts. The bottom panels shows the pixels in the corresponding maps $\kappa_{n,F}(x, y)$, noised and smoothed with $\theta_F = 1$ arcmin to account for observational effects with $f_\sigma \geq 1$ [3]

We characterise the peak properties for a given threshold f_σ as following: (*i*) we identify all the pixels above f_σ times the noise level, (*ii*) we join them to the same peak group using a two-dimensional friend-of-friend approach adopting the pixel scale as linking length parameter, (*iii*) we define the coordinate of the peak centre according to the location of the pixel with the maximum value and the area as related to the number of pixels that belong to the group times the pixel area; we term our peak identification algorithm TwinPeaks[4]: while for small values of the signal-to-noise threshold f_σ some peaks are twins, for large values of f_σ they become distinct and isolate. We want to emphasise that, as discussed, the peak identification method depends on the resolution of the convergence map – constructed from simulations or reconstructed using the shear catalogue of an observed field of view. Being interested in displaying and discuss relative differences in the counts and in the properties of the peaks for various Dark Energy models, all the maps have been created to have the same pixel resolution: field-of-view of 5 deg by side are resolved with 2048×2048 pixels, consistently noised and smoothed using the same parameter choices.

3 WEAK LENSING PEAK PROPERTIES IN COUPLED DM-DE MODELS

We run the complete and self-consistent TwinPeaks pipeline on all light-cones generated for the various cosmological models: ΛCDM, EXP003, EXP008e3, SUGRA and ΛCDM – HS8. In all cases we have considered two fixed source redshifts $z_s = 0.75$ and $z_s = 1.12$ (that are the median source redshifts of the two considered source redshift distributions) with a number density of galaxies of 18 and 33 per square arcmin for the ground- and space-based observations, respectively. As an example, in Figure 4 we display the TwinPeaks results for light-cones derived from the same random realisation of initial conditions at $z = 99$ for the five different cosmological models, colour coded as displayed in the figure legend: black, blue, orange, red and green refer to ΛCDM, EXP003, EXP008e3, SUGRA003 and ΛCDM – HS8, respectively. In this case, we show the results for $z_s = 1.12$; in each panel the three gradations of colours mark the regions which are 1, 3 and 5 times above the noise level, considering a filter size $\theta_F = 1$ arcmin.

3.1 Peak Counts

Figure 5 displays the fraction of the area occupied by peaks as a function of the signal-to-noise level f_σ, for the various cosmologies. Each curve corresponds to the average value computed on the 25 different light-cone realisations. Left and right panels display the results for a ground and space analysis, respectively. The outcomes for the various cosmological models are shown using different colours. The grey region bracketing the measurements of the ΛCDM model (black curve) shows the variance of the different light-cone realisations. The variance for the other models is similar and then not shown for clarity reasons. The corresponding bottom panels present the relative difference in the measured area in peaks with respect to the reference ΛCDM model as a function of the signal-to-noise value f_σ. The green diamonds show the predictions from our halo model formalism for the standard ΛCDM model, described in more details in the Appendix. We notice that the model describes quite well the predictions of the corresponding cosmological model, it captures within few percents the behaviour for large values of the signal-to-noise ratio. The blue crosses (present only on the right panel) show the results of our model where we also include the presence of subhaloes. As described by Giocoli et al. (2017) we treat them as Singular Isothermal Spheres. From a more detailed analysis we highlight that subhaloes boosts the weak lensing peaks at most 3 percent. This is due to two main reasons: (*i*) subhaloes are typically embedded in more massive haloes whose contribution to the convergence map is stronger and (*ii*) their presence may be washed out by the noise and the smoothing of the convergence map. From the bottom panels we see that the higher peaks allow for a better discrimination between different cosmological models, while for low values of f_σ the peaks trace mainly projected systems and filaments. At about $f_\sigma = 6$ the two most extreme models EXP003 and ΛCDM – HS8 show a positive difference of about 15 – 20% while at $f_\sigma = 10$ - attainable for a space observation with a large number density of background galaxies – of approximately 25 – 30%, in the regime where peaks are not dominated by the shape noise. The fraction of area in peaks for the EXP008e3 and SUGRA models are situated at almost 1 σ away from the ΛCDM one. It has also been pointed out by Maturi et al. (2010) who showed that weak-lensing peak counts are dominated by spurious detections up to signal-to-noise ratios of 3 – 5 and that large scale structure noise can be suppressed using an optimised filter. For large f_σ we detect the non-linear scales (typically for angular modes with $l > 10^2$) where galaxy clusters are located, making peak statistic complementary to cosmic shear measurements (Shan et al. 2017). We can also see that observations from space should resolve peaks with a much higher resolution than ground-based ones and also resolve peaks with much higher signal-to-noise ratio where the difference

[2] We remind the reader that our distributions are supposed to mimic, in an optimistic way, a space- and ground-based experiment; in addition we point out that the source redshift distribution for the Euclid ESA Mission (Kitching et al. 2016) is expected to have a median redshift of galaxies for shape measurement $z_m = 0.9$.

[3] Contrary to many peak studies we choose to indicate the peak height above the noise with f_σ instead of ν since the latter is typically used in some of our previous works for $\delta_c^2(z)/\sigma^2(M)$.

[4] https://www.youtube.com/watch?v=V0cSTS2cTmw.

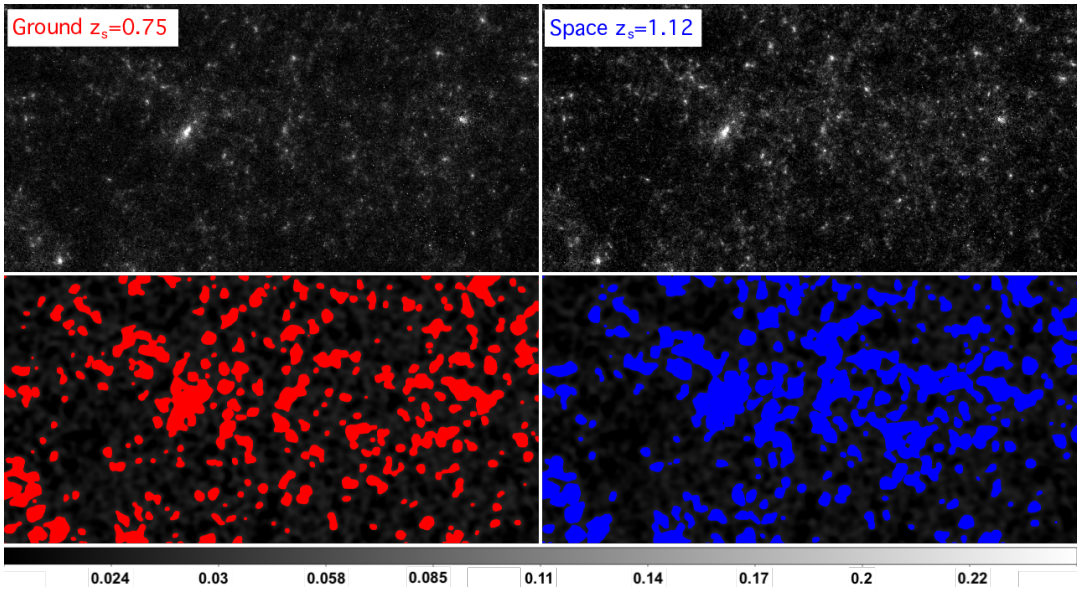

Figure 3. Top panels: convergence maps for one light-cone realisation of the ΛCDM simulation assuming sources at two fixed redshifts – corresponding to the median redshifts for the space- and ground-based redshift distributions here considered. Bottom panels: pixels above the corresponding noise level $\sigma_{\rm noise}$. The scale of the field-of-view along the x-axis of the displayed regions is approximately 3 degrees large.

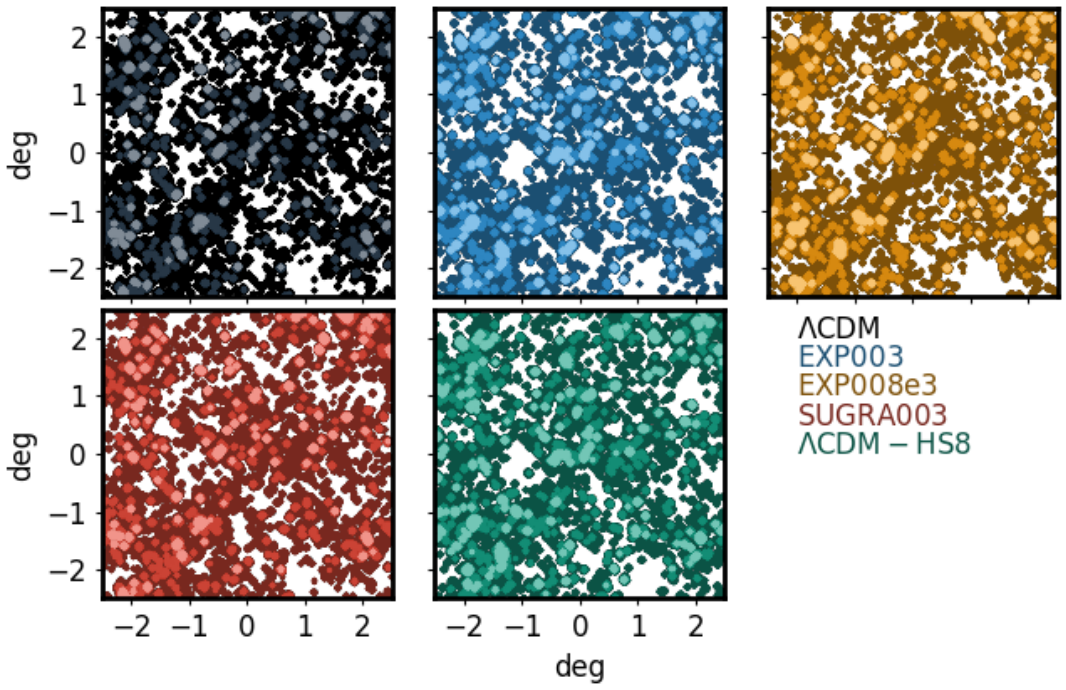

Figure 4. Examples of the weak lensing peak locations in the different cosmological models, from the map computed assuming a space source redshift distribution with z_s = 1.12. The maps include shape noise and are smoothed with a Gaussian filter with scale θ_F = 1 arcmin. The different coloured panels show various cosmological models as indicated in the label. Within each panel the three gradations of colour mark the regions in the field-of-view which are 1, 3 and 5 times above the expected noise level $\sigma_{\rm noise}$.

between the various cosmological models is largest. Comparing the figure with the cosmic shear forecast analyses on the same cosmological models by Giocoli et al. (2015) we notice that high signal-to-noise peak statistics is able to differentiate more the various dark energy models. This suggests that future wide field surveys like Euclid will be excellent for this type of analyses, binding much more the cosmological models not only in the Ω_m-σ_8 planes but also in the dark energy equation of state.

In Figure 6 we display the number of peaks above a given threshold of the signal-to-noise level; data points and colours are the same as in Fig. 5. From the figure we notice that the trend of the peak counts is very similar to that of the area in peaks as previously discussed. The ΛCDM – HS8 is very distinct from the ΛCDM model in peak counts, showing also a different behaviour with respect to the EXP003 model which has the same power spectrum normalisation. Peak statistics traces the different growth of structures and expansion histories. From the bottom panels we can notice that the ΛCDM model with high σ_8 predicts much more weak lensing peaks: this model has much more haloes which are much more concentrated due to their higher formation redshift. In general a higher peak abundance in weak lensing fields is mainly due to a combined effect of the projected halo mass function in the light-cones and to the redshift evolution of the mass-concentration relation.

Results presented until now considered sources located at a fixed redshifts. However weak lensing tomographic analyses provide the possibility of tracing the structure formation process as a function of redshift and can be an important constraint on the growth factor and on the dark energy equation of state. This can be possible as long as we have a reasonable number of background galaxies per redshift bin. In order to perform a weak lensing peak analysis as a function of redshift, both for the space- and ground-based cases we divide the corresponding source redshift distribution in three redshift bins that contain one-third of the total expected number density of galaxies. As mentioned before those bins in redshift are displayed with different colour gradations in Figure 1. In Figure 7 we present the fraction of the area in peaks above a given threshold $f_\sigma = 3$ as a function of the source redshift for the various cosmological models and the two experiments: from ground (left) and space (right): they have 6 and 11 galaxies per arcmin^2 per bin, respectively. For the space case we also show the measurement for high peaks with $f_\sigma = 5$ (dashed lines), that are not properly resolved for the ground based experiment because of the low number density of background sources. The black error bar corresponds to the rms in the measurements for the reference ΛCDM model. The tomographic peak analysis illustrates the capability of following the structure formation processes for the different cosmological models. While for the ground-based case the maximum redshift considered is $z \approx 1.1$, from space we can go up to $z \approx 2.3$. As in the previous discussions both the EXP003 and ΛCDM – HS8 present the largest differences in peaks with respect to the reference ΛCDM model. For example the right panel displays that the SUGRA003 model has at high redshift an area in peaks very similar to the ΛCDM cosmology, while at low redshifts (as it can also be noticed in the left panel) the area in peaks is larger than the corresponding one in the standard model. This is actually consistent with the fact that SUGRA003 is a bouncing model characterised by a different evolution of both the growth factor and the Hubble function (see Baldi 2012a). Tomographic peak statistics will be a powerful tool for discriminating dark energy models from standard cosmological constant, being able to self-consistently trace the growth of structures, and more specifically – as we will discuss in the next section – of galaxy clusters as a function of the cosmic time.

4 GALAXY CLUSTERS AND WEAK LENSING PEAKS

The results presented in the last section show that weak lensing peaks tend to be located close to high-density regions of the projected matter density distribution and that simulations based on the halo model describe quite well both the peak area and number counts as a function of the signal-to-noise ratio. The fact that the contribution of subhaloes to the weak lensing peaks is negligible also suggests that clusters, and line-of-sight projections of haloes, represent the main contribution to high peaks in the convergence maps.

In this section we will discuss the correlation between peaks and galaxy clusters present within the simulated light-cones, and try to shed more light on the connection between high peaks and massive haloes. We tag a halo as a contributor to a peak if its centre of mass has a distance smaller then 1 pixel from a peak above a certain signal-to-noise value f_σ.

In Figure 8 we display the cumulative halo mass function per square degree within the constructed light-cones, for the various cosmological models, up to $z = 0.75$, $z = 1.12$ and $z = 4$ from left to right, respectively. For the halo mass we use M_{200}, the mass enclosing 200 times the critical density of the universe at the same redshift. For comparison, in each panel the light-blue and dark-grey curves display the predictions by Despali et al. (2016) and Tinker et al. (2008) for the M_{200} mass definition. The bottom panels show the relative difference of the counts with respect to the measurement in the standard ΛCDM simulation. From these panels we can notice that the integrated halo mass function of the SUGRA003 model is very similar to the ΛCDM (the SUGRA003 model has been actually constructed to result in such similarity at low redshifts, see Baldi et al. 2011, for a detailed discussion on this issue). However the number of peaks in this model is quite different (as shown in Fig. 5 and 6) and comparable to the peak counts in EXP008e3. This is a clear signature of the halo properties (Cui et al. 2012; Giocoli et al. 2013): clusters in the bouncing SUGRA003 model form at higher redshifts and are typically very concentrated. This translates in higher and more numerous peaks in the convergence field. This is a confirmation that peak statistics is very sensitive not only to the initial power spectrum but also to the non-linear processes that characterise halo formation histories and that may help disentangling models that would appear degenerate in other observables as the halo mass function. This is in agreement with the finding obtained by Shan et al. (2017): peak statistics gives complementary constraints with respect to cosmic shear in the $\sigma_8 - \Omega_m$ plane, and in this case, as we have shown, also in the extended parameter space of coupled Dark Energy cosmologies.

The three panels in Figure 9 show the redshift distribution of clusters in the light-cones with mass $M_{200} \geq$

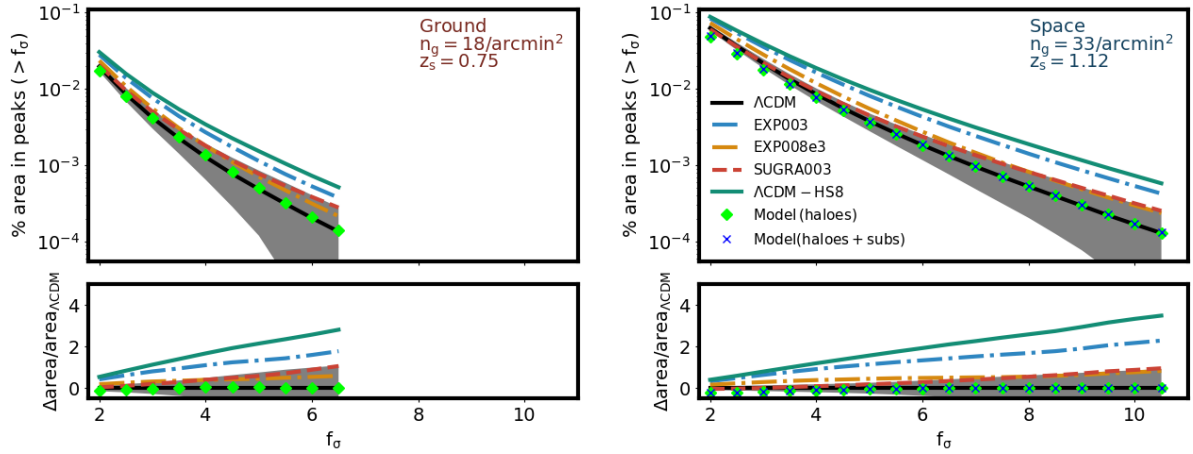

Figure 5. Left and right panels show the fraction of the area covered by weak lensing peaks as a function of the threshold of the noise level, for the various cosmological models for a space and a ground based source redshift distribution, respectively. The grey area bracketing the black lines shows the variance of the different light-cone realisations for the ΛCDM model. The various coloured curves display the measurement done on the light-cones of the different cosmological models. Green diamonds and blue crosses display the predictions obtained using our halo and halo plus subhalo models, discussed in the Appendix.

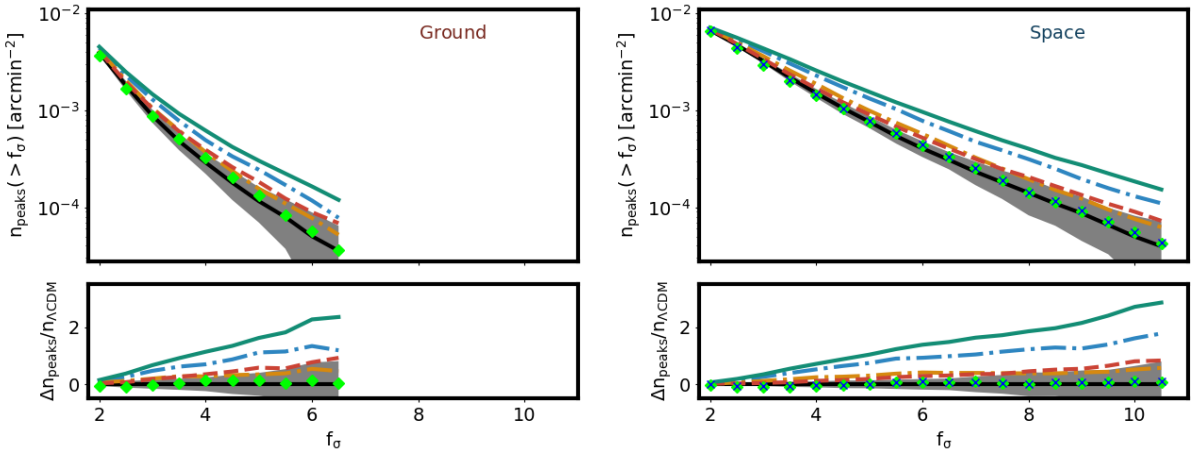

Figure 6. Peak counts above a given noise f_σ level for the various cosmological models. Data points, lines and panels are as in Figure 5.

$10^{14} M_\odot/h$ as a function of redshift. Left and central panels display the redshift distribution of systems that fall into peaks with $f_\sigma = 2$ for the ground- and space-based experiment, respectively; the right panel, instead, shows the distribution of the whole cluster population within the constructed past-light-cones. Dashed and solid vertical lines mark $z_s = 0.75$ and $z_s = 1.12$, respectively. In these figures it is possible to see that the number of clusters in the SUGRA003 model is quite similar to ΛCDM one while large differences are present in the counts with respect to the ΛCDM with high σ_8 and EXP003.

Top and bottom panels in Figure 10 display the fraction of clusters corresponding to weak lensing peaks for space- and ground-based experiments, respectively. In both panels we show the fraction of clusters in peaks above various weak lensing noise levels, for the different cosmological models, colour coded as in the other figures. The considered source redshifts for the space- and ground-based experiments are $z_s = 0.75$ and $z_s = 1.12$, respectively, and that those also correspond to the maximum cluster redshift we consider; moreover we consider clusters with masses above $M_{200} \geq 10^{14} M_\odot/h$. We notice that for the space experiment we find that almost 55% (70%) of the clusters with $z < 1.12$ are in peaks 3 (2) times above the noise level, while for the ground-based experiment it is nearly 30% (50%) of all clusters with $z < 0.75$. We remind the reader that for a cluster to be within a peak it is necessary that its projected centre of mass falls in a pixel of the corresponding map that is above the desired threshold: by definition each peak, depending on its shape, may or not contain more than a halo with $M_{200} \geq 10^{14} M_\odot/h$. The halo contribution to the corresponding weak lensing field is weighted by the lensing distance $D_{lens} \equiv D_{ls} D_l / D_s$ (where D_l D_s and D_{ls} are the angular diameter distances observer-lens, observer-source and source-lens, respectively) so that haloes, even if they have the same mass, contribute differently to the lensing signal depending on their redshift: for example, considering $z_s = 1.12$ the lensing distance D_{lens} peaks around $z = 0.38$. This is more evident in Figure 11 where we show the fraction of clusters with $z \leq 0.5$ in peaks above different thresholds of the

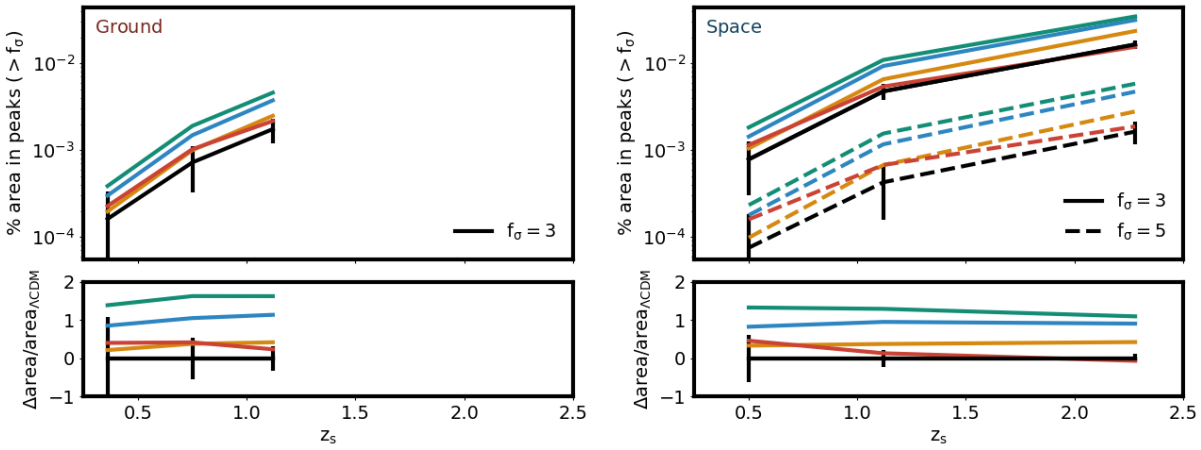

Figure 7. Fraction of the area in peaks as a function of the source redshift for space- (left) and ground-based (right) observations. Solid lines show the area above 3 times the noise level, while the dashed ones consider peaks above $f_\sigma = 5$. In particular for the ground-based experiment we display only the case for $f_\sigma = 3$ since peaks with higher values of the noise are poorly resolved because of the number density of 8 galaxies per arcmin^2, per redshift bin. Various colours refer to the different cosmological models, as indicated in previous figures.

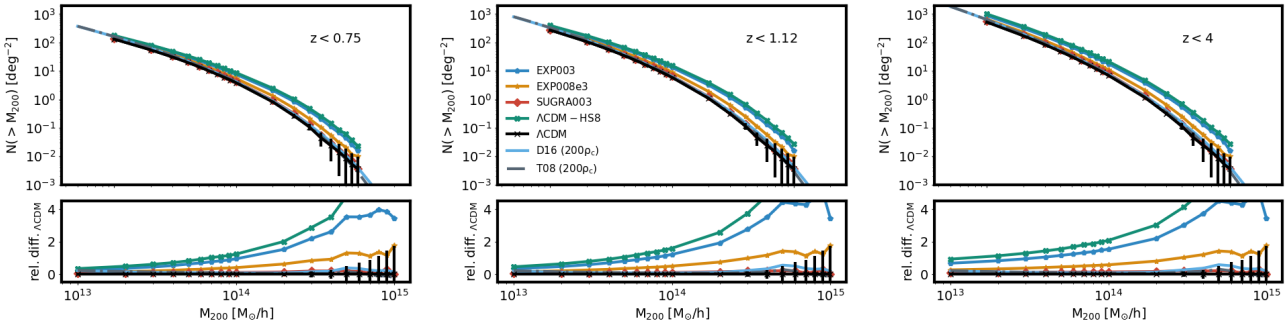

Figure 8. Halo mass function per square degree within the simulated light-cones up to redshifts $z = 0.75$, $z = 1.12$ and $z = 4$ from left to right respectively. The data points show the measurements in the various cosmological models – with Poisson error bars displayed only for the ΛCDM model. The light-blue and dark-grey curves show the predictions from the Despali et al. (2016) and the Tinker et al. (2008) mass function for the ΛCDM cosmology.

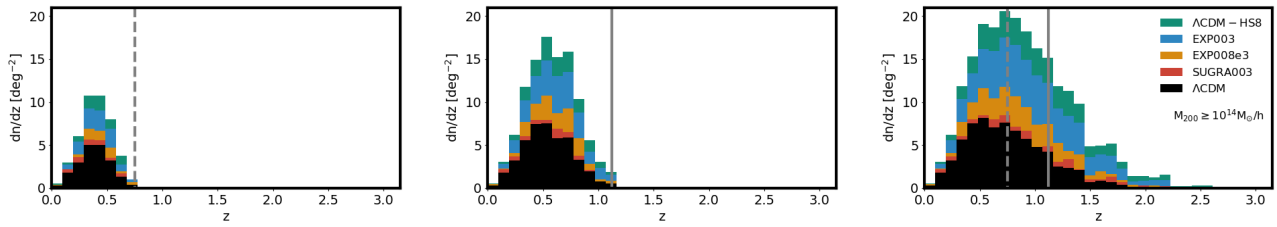

Figure 9. Differential number density of clusters with $M_{200} \geq 10^{14} M_\odot/h$ per unit of square degree for the various cosmological models. Left and central panels show the redshift distributions of clusters in peaks with $f_\sigma = 2$ for the ground and space experiments, respectively. Right panel displays the redshift distribution of clusters for each cosmological model within our constructed light-cones. Solid and dashed vertical lines show the source redshift for the two considered cases ground and space-based: $z_s = 0.75$ and $z_s = 1.12$, respectively.

noise level, for the space case. The fraction of haloes with $M_{200} \geq 10^{14} M_\odot/h$ and $z \leq 0.5$ in peaks with $f_\sigma = 2$ is close to unity. The arrow on each data point shows the corresponding fraction of clusters in peaks when we select systems with $z \leq 0.38$ – the peak of the lensing kernel for $z_s = 1.12$.

The correlation between weak lensing peaks (above a given threshold) and clusters represents a promising statistics to identify regions in the plane of the sky where clusters are more likely to be found. In Figure 12 we display the normalised cumulative distribution of the angular distances $\Delta\theta_{\rm cl,peak}$ between the cluster centre of mass and the location of the closest pixel with the highest value of the convergence with $f_\sigma = 2$. The black shaded histogram shows the cumulative distribution of distances $\Delta\theta_{\rm cl,peak}$ in arcmin for the ΛCDM light-cones for sources and clusters up to $z = 1.12$, while the green lines refers to the halo model predictions when weak lensing maps are produced using our fast weak lensing model (see Appendix). The relative differ-

Table 2. Number of clusters with $M_{200} \geq 10^{14} M_{\odot}/h$ (with $z < 1.12$, second and third columns, and $z \leq 0.5$, forth and fifth columns) in peaks above the threshold of $f_{\sigma} = 2$ in the various cosmological models. Second and fourth columns display the number of clusters in the various models up to redshift 1.12 and 0.5, respectively. On the other side, third and fifth columns present the corresponding cluster counts in peaks with signal-to-noise ratio $f_{\sigma} = 2$, while the number between parentheses refers to the number of clusters in peaks for which the centre of mass corresponds with the pixel with the highest value. Numbers refer to the sum over 25 different light-cone realisations, for a total of 625 sq. deg., for each cosmology.

	n. cl. $z < 1.12 \rightarrow$	n. cl. in peaks (with $\Delta\theta_{\rm cl,peak} = 0$)	n. cl. $z \leq 0.5 \rightarrow$	n. cl. in peaks (with $\Delta\theta_{\rm cl,peak} = 0$)
ΛCDM	3730	**2655 (90)**	1207	**1188 (53)**
EXP003	8223	5460 (158)	2130	2088 (83)
EXP008e3	5523	3834 (102)	1602	1576 (57)
SUGRA003	4069	2926 (130)	1314	1308 (77)
ΛCDM – HS8	9684	6410 (191)	2429	2391 (110)
Model	*3730*	**2634 (124)**	*1207*	1201 (69)

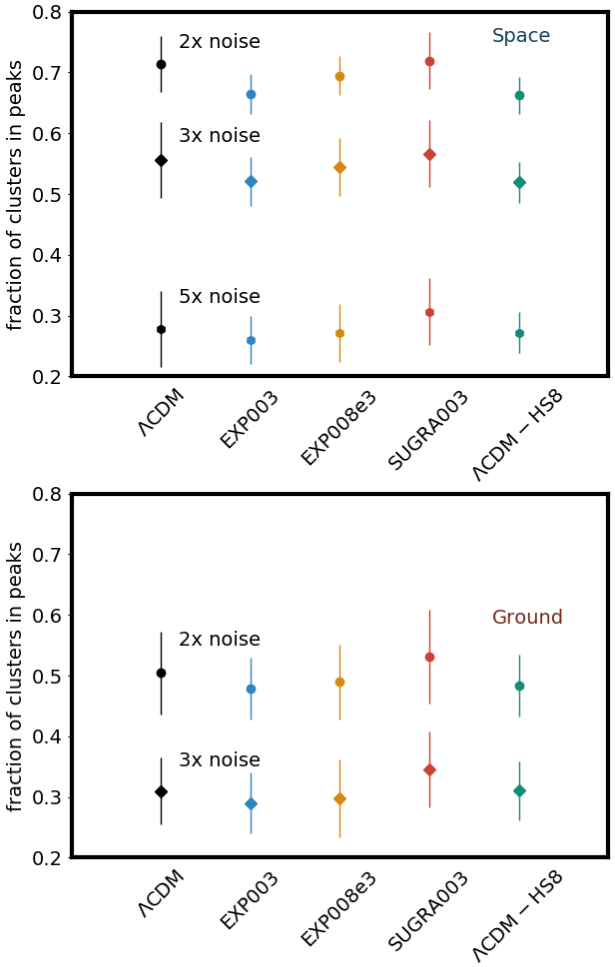

Figure 10. Fraction of clusters in peaks for a space- and ground-based analysis of the weak lensing simulations (top and bottom panel respectively) for the various cosmological models considered in this work. In the top panel we consider all the clusters with $M_{200} \geq 10^{14} M_{\odot}/h$ up to the source redshift of $z_s = 1.12$, while in the bottom panel up to $z_s = 0.75$. Different data points display the fractions of those systems whose centre of mass falls within high convergence pixels which are part of weak lensing peaks above a given threshold value f_{σ}.

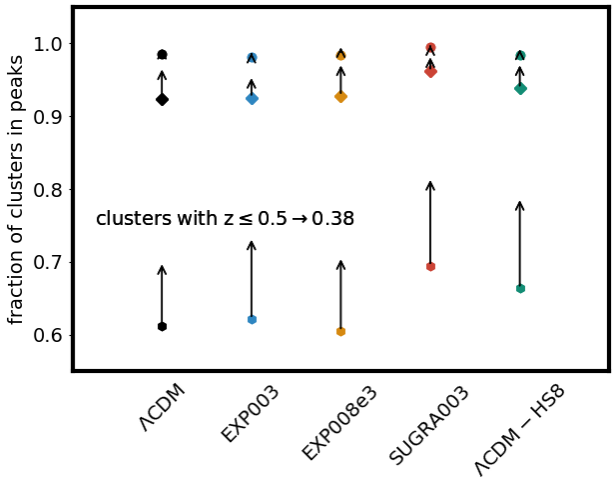

Figure 11. Fraction of clusters for a space-based analysis with $M_{200} \geq 10^{14} M_{\odot}/h$ and $z \leq 0.5$ in peaks with convergence values above $f_{\sigma} = 2$, 3 and 5 from top to bottom data points, respectively. The arrow on each data point shows the corresponding fraction of clusters in peaks when we select systems with $z \leq 0.38$ – the peak of the lensing kernel for $z_s = 1.12$.

ence between those two histograms remains well below 10% and both distributions converge to unity around 7 arcmin. Nonetheless, peaks in the convergence maps created using all the particles from the simulations have slightly misaligned centres and less correlation with cluster centres than peaks in the halo model maps because of the filamentary structure present in the convergence field. This manifests also in the fact that peaks are not spherical but typically elliptical. The magenta histogram displays the case of clusters with $z \leq 0.5$, that, as we will discuss later, contribute the most to the convergence peaks with $f_{\sigma} = 2$ and $z_s = 1.12$. The vertical grey line indicates the angular scale of the pixel of the convergence maps. From the figure we notice that less than five percent of the clusters have a centre of mass that overlaps with the highest peak, approximately seventy percent are closer than one arcmin to the highest peak while all clusters are within 7 arcmin from some peak. In order to see how the correlation between clusters and peaks compares with respect to random points, in red we display the cumulative distribution of the distance between clusters and peaks, when

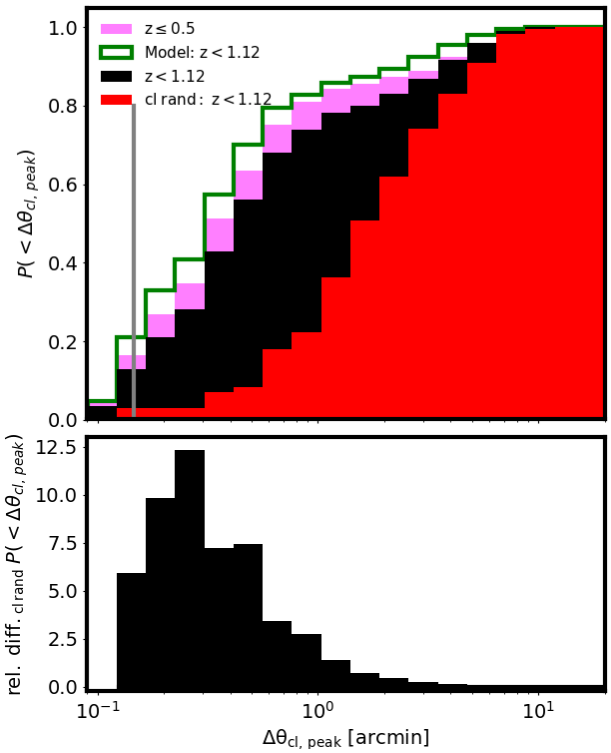

Figure 12. Normalised cumulative distribution of the distance between the centre of mass of the clusters in peaks and the closest pixel with highest value. The results refer to the ΛCDM cosmology. This result does not have important cosmological dependence, all the other models possess a similar distribution. The vertical grey line indicates the angular scale corresponding to the pixel size in the convergence map. The green histogram refers to the measurements with respect the convergence maps constructed using our fast weak lensing halo model formalism, discussed in details in the Appendix. The red histogram shows the cumulative distribution of the distance between peaks and clusters, when the latter are assumed to have random position within the field-of-view. The bottom panel displays the relative difference between the black and the red histograms.

the former are assumed to have random positions within the field-of-view. The relative difference between the two distributions clusters-peaks and random clusters-peaks (black and red histograms, respectively) is displayed in the bottom panel. In this panel we can notice in more details that at small scales clusters and peaks are more correlated than random cluster positions which has a maximum at about 15 arcsec.

In Table 2 we summarise our results about the correspondence of weak lensing peaks and clusters within the simulated past light-cones. Each row refers to a different cosmological model, while the last one reports the findings in our halo model simulated fields for the ΛCDM cosmology. The numbers correspond to the 25 different light-cone realisations for each model for a total of 625 square degrees.

5 SUMMARY & CONCLUSIONS

In this work we have investigated the weak lensing peak statistics and properties in a set of light-cones constructed from the coupled DM-DE simulations of the CoDECS suite. In particular we have studied how the number density and area of weak lensing peaks differ between models using typical source redshift distribution from ground and space observations. In what follows we summarise our main findings:

- the various cosmological models display different peak counts that increase with the signal-to-noise ratio f_σ. The extreme model EXP003 for $f_\sigma = 10$ displays a relative difference of about 20% with respect to the ΛCDM and exhibits a different behaviour with respect to the ΛCDM – HS8 which has the same power spectrum normalisation;
- the fraction of area on the sky in peaks as a function of the signal-to-noise ratio displays a behaviour similar to that of the peak counts, except that for small values of f_σ we found twin-peaks above a given threshold while for large values of f_σ high convergence regions are isolated and become more distinct with respect to the projected linear and non-linear large scale matter density distribution; the relative difference between EXP008e3 and SUGRA003 in peak area is reversed with respect to peak counts underlining the importance of the concentration-mass relation in peak statistics;
- weak lensing peaks reflect the non-Gaussian properties of the underlying projected density field, trace non-linear structure formation processes and are very sensitive to the evolution of dark energy through the growth of density perturbations and the geometry of the expansion history. This confirms the idea that weak lensing peak statistics, and their tomographic analysis, can provide complementary information to cosmic shear analysis alone;
- peak abundance and properties are due to non-linear structures present along the line-of-sight and projected matter density distribution; in particular high signal-to-noise peaks are mainly produced by galaxy clusters and for the source redshift distribution as expected from a space-based experiment we find that almost the whole cluster population up to $z = 0.5$ is in peaks with signal-to-noise ratio $f_\sigma = 2$;
- only five percent of the clusters have their centres of mass within the highest pixel in a peak of the convergence map (resolution 8.8 arcsec). On the other hand, all clusters are located within 7 arcminutes of the maximum convergence pixel of a peak;
- our halo model formalism for creating fast weak lensing simulations describes well the abundance of peaks for the different source redshift distributions;
- the inclusion of substructures in our halo model raises the peak statistics only by a few percent;

Weak lensing peak statistics represents a powerful tool for characterising non-Gaussian properties of the projected matter density distribution. Peak properties depend on dark energy and their tomographic analysis allows one to trace the structure formation processes as a function of the cosmic time. Our results underline the necessity of combining peak statistics with other cosmological probes: this will offer important results from upcoming wide field surveys and will push cosmological studies toward new frontiers.

ACKNOWLEDGMENTS

CG and MB acknowledge support from the Italian Ministry for Education, University and Research (MIUR) through the SIR individual grant SIMCODE, project number RBSI14P4IH. All authors also acknowledge the support from the grant MIUR PRIN 2015 "Cosmology and Fundamental Physics: illuminating the Dark Universe with Euclid". We acknowledge financial contribution from the agreement ASI n.I/023/12/0 "Attività relative alla fase B2/C per la missione Euclid". MM and CG acknowledge support from the Italian Ministry of Foreign Affairs and International Cooperation, Directorate General for Country Promotion. We thank also Federico Marulli and Alfonso Veropalumbo for useful discussions. We are also grateful to the anonymous reviewer for her/his useful comments.

APPENDIX A: FAST HALO MODEL SIMULATIONS AND A MODEL FOR WEAK LENSING PEAKS

Modelling peak statistics represents a significant challenge when using peak counts as complementary cosmological probe to cosmic shear power spectrum. Predicting peaks in weak lensing convergence maps can be done assuming that non-linear structures, like dark matter haloes, are the main contributors to high-significance peaks. In this paper we have shown that while haloes hosting galaxy clusters are the main contributors to high peaks, projection effects from small haloes aligned along the line-of-sight contribute to peaks with low signal-to-noise ratio.

In this appendix we will show that peaks identified in convergence maps constructed using fast weak lensing simulations with WL-MOKA (Giocoli et al. 2017) are in very good agreement with those in maps computed from full particle ray-tracing simulations. Fast halo model simulations could prove extremely useful by reducing the computational requirements for N-body simulations by some orders of magnitude both in cosmic shear power spectrum and peak statistics (Lin & Kilbinger 2015a,b; Zorrilla Matilla et al. 2016) when combined with approximate simulation methods like COLA (Izard et al. 2018) and PINOCCHIO (Monaco et al. 2013; Munari et al. 2017; Monaco 2016). As discussed by Giocoli et al. (2017) on a single light-cone simulation, our fast halo model method is approximately 90 per cent faster than a full ray-tracing simulation using particles. However, it should be stressed that an N-body run of 1 Gpc/h with 1024^3 collisionless particles from $z = 99$ to the present time using the GADGET2 code (Springel 2005) takes around 50 000 CPU hours, while a run with an approximate method may take approximately 750 CPU hours to generate the past-light cone up to the desired maximum redshift $z = 4$.[5]

The theoretical approach for weak lensing peak prediction is based on the projected halo model formalism (Cooray & Sheth 2002). A full characterisation of the halo population along the line-of-sight, with consistent clustering properties, gives us the possibility of predicting not only the peaks in cluster regions but also those in the field , mainly due to projected interposed mass density distribution.

In order to build our peak model, in addition to the convergence maps constructed using the particles from the numerical simulations, for the ΛCDM model we also use a sample of maps computed using the halo properties as presented in Giocoli et al. (2017). In order to do so, we use the corresponding projected halo and subhalo catalogue from MapSim, considering all friends-of-friends groups above the resolution $M > 2.1 \times 10^{12} M_{\odot}/h$. Each halo, as read from the simulation catalogue and present within the considered light-cone field-of-view, is assumed to be spherical and characterised by a well defined density profile (Navarro et al. 1996) (hereafter NFW). We assume the halo concentration c to be mass and redshift dependent as in Zhao et al. (2009) in which we imply the mass accretion history model by Giocoli et al. (2012b) and we assume a log-normal scatter in concentration for fixed halo mass of $\sigma_{\ln c} = 0.25$ consistent with the results of different numerical simulations (Jing 2000; Dolag et al. 2004; Sheth & Tormen 2004; Neto et al. 2007). In this case we can compute the convergence map by integrating the halo profile along the line-of-sight up to the virial radius that can be read as:

$$\kappa(x, y) = \int_{-R_{vir}}^{R_{vir}} \rho(x, y, z) \mathrm{d}z / \Sigma_{\rm crit}\,, \tag{A1}$$

where

$$\Sigma_{cr} \equiv \frac{c^2}{4\pi G} \frac{1}{D_{lens}} \tag{A2}$$

is the critical surface mass density. For the NFW profile and assuming that along the line-of-sight we can integrate up to infinity, equation (A1) can be simplified to (Bartelmann 1996):

$$\kappa_{NFW}(x, y) = \frac{2\rho_s r_s}{\zeta^2 - 1} \frac{F(\zeta)}{\Sigma_{\rm crit}}\,, \tag{A3}$$

where $\zeta \equiv \sqrt{(x^2 + y^2)}/r_s$, $r_s = R_{vir}/c$, and:

$$F(\zeta) = \begin{cases} 1 - \frac{2}{\sqrt{\zeta^2 - 1}} \arctan \sqrt{\frac{\zeta - 1}{\zeta + 1}} & \zeta > 1, \\ 1 - \frac{2}{\sqrt{1 - \zeta^2}} \mathrm{arctanh} \sqrt{-\frac{\zeta - 1}{\zeta + 1}} & \zeta < 1, \\ 0 & \zeta = 1. \end{cases}$$

Left and right panels of Fig. A1 show the convergence maps for $z_s = 1.12$ of one light-cone realisation of the ΛCDM model using particles and haloes, respectively. The top panels show the convergence maps for $z_s = 1.12$ while in the bottom we have includeed random noise assuming a number density of galaxies $n_g = 33$ arcmin^{-2} and the maps have been convolved with a Gaussian filter with $\sigma_F = 1$ arcmin. In white, red and yellow we display the regions in the maps that are 1, 3 and 5 times above the noise level. From the figure we notice that qualitatively the peak location is very similar: the most massive haloes are responsible for the highest convergence peaks, regions with few systems appear, in projection, under-dense. However the shapes of the peaks in the right panel are quite spherical as the haloes used in the construction are, however the halo locations correlate with the peaks as well as with the large scale matter density distribution (Despali et al. 2014; Bonamigo et al. 2015; Despali et al. 2017).

[5] All the CPU times given here have been computed and tested in a 2.3 GHz workstation.

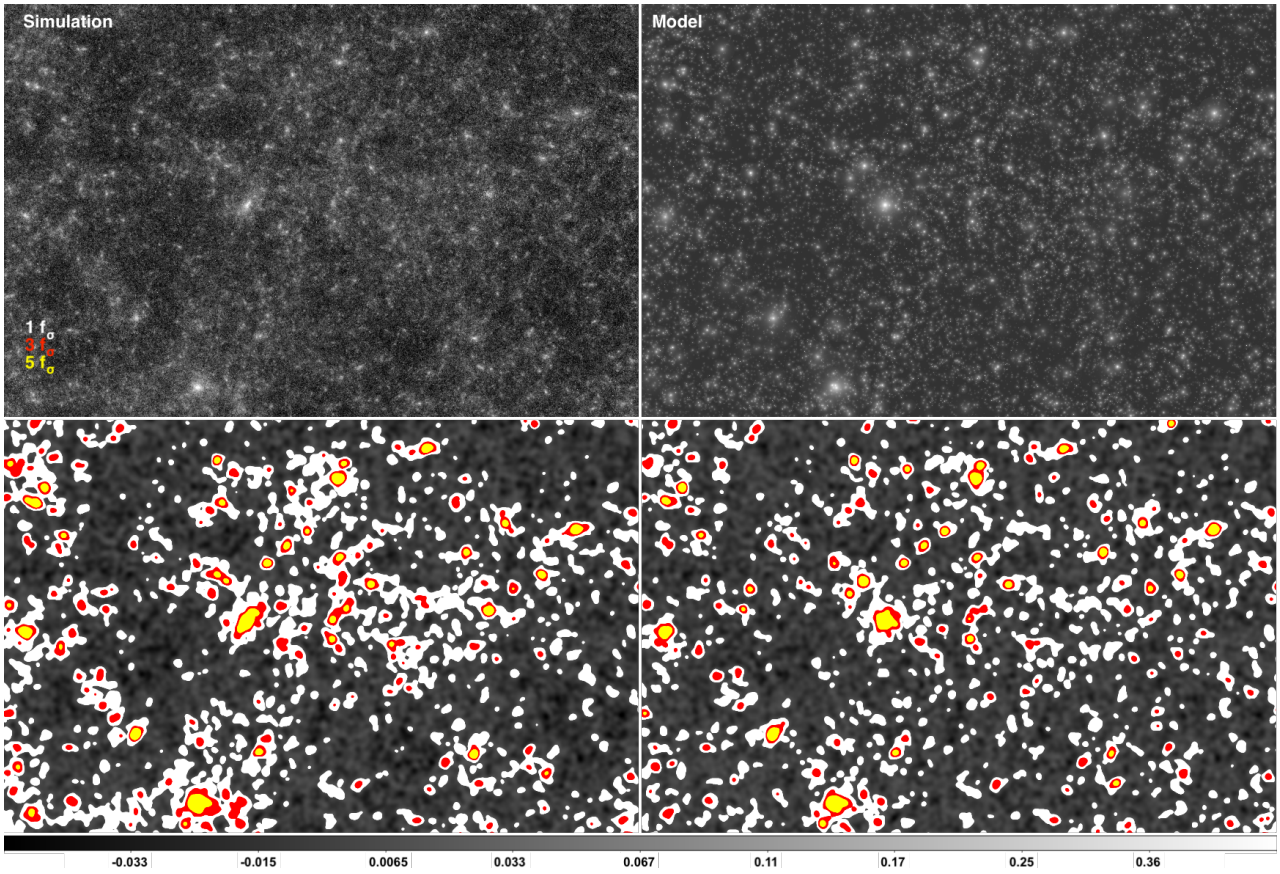

Figure A1. Top panels: convergence maps for source redshift $z_s = 1.12$. In the left panel we show the map computed using all particles within the light-cone while on the right we display the reconstruction performed using all haloes with friends-of-friends mass larger than $2.1 \times 10^{12} M_\odot/h$. Bottom panels: peak detection in convergence maps created using particles (left) and haloes (right) from the same light-cone realisation of the ΛCDM simulation. The convergence map has been constructed assuming $z_s = 1.12$, noised and smoothed assuming $\sigma_F = 1$ arcmin and 33 galaxies per square arcmin. In white, red and yellow we display the pixels in the map which are 1, 3 and 5 times above the noise level.

In producing the lensing simulation model using haloes we have been consistent in taking the halo positions from the simulation, and projecting them on the plane of the sky. This means that up to the simulation scale of 1 Gpc/h the clustering of the systems is preserved. However one may ask if this has a direct impact on the peak counts of the constructed convergence maps. In order to understand this for each halo model light-cone we have created 16 realisations where we have preserved the halo masses and concentrations but we have assigned to each halo a random position within the field of view. In Figure A2 we display the relative number counts and area in peaks as a function of the signal-to-noise level f_σ between the halo model simulation when positions are read from the simulation and when they are randomly assigned. We show the results both for a space- and ground-based analysis displayed in blue and red, respectively. The figure shows that proper halo positions are necessary for a good characterisation of the peak statistics mainly for high values of the noise level. These allow a good description of the large scale density distribution and of the effect of correlated and uncorrelated structures on the location of high density regions. From the figure we can see that for large values of the noise level the relative difference in the area and in the number of peaks tends to 10% and that in the upper panel already for $f_\sigma = 2$ the relative difference is about 5%.

This paper has been typeset from a TEX/LATEX file prepared by the author.

References

Amara A., Lilly S., Kovač K., Rhodes J., Massey R., Zamorani G., Carollo et al. 2012, MNRAS, 424, 553
Baldi M., 2012a, Physics of the Dark Universe, 1, 162
Baldi M., 2012b, MNRAS, 422, 1028
Baldi M., Pettorino V., Amendola L., Wetterich C., 2011, MNRAS, 418, 214
Baldi M., Pettorino V., Robbers G., Springel V., 2010, MNRAS, 403, 1684
Bartelmann M., 1996, A&A, 313, 697
Bartelmann M., Schneider P., 2001, Physics Reports, 340, 291
Bellagamba F., Meneghetti M., Moscardini L., Bolzonella M., 2012, MNRAS, 422, 553
Benjamin J., Van Waerbeke L., Heymans C., Kilbinger M., Erben T., Hildebrandt H., Hoekstra H., et al. 2013, MNRAS, 431, 1547
Bertin E., Arnouts S., 1996, A&AS, 117, 393

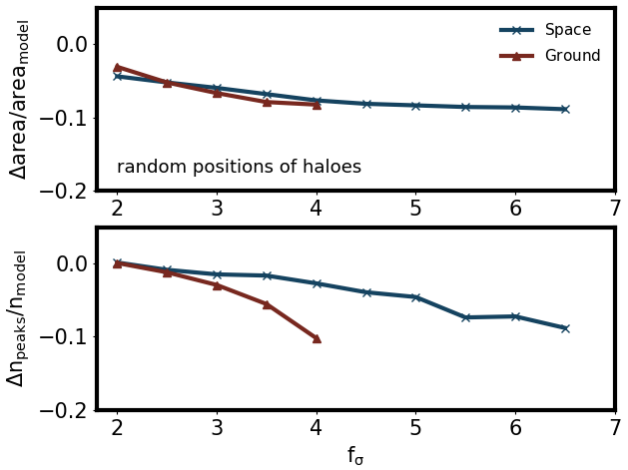

Figure A2. Relative peak area and counts as a function of the noise threshold, from our fast lensing halo model, when the halo positions are read from the simulation and defined to be random. The red and blue data points show the results considering a space or a ground based analysis, respectively.

Betoule M., Kessler R., Guy J., Mosher J., Hardin D., Biswas R., Astier P., et al. 2014, A&A, 568, A22

Boldrin M., Giocoli C., Meneghetti M., Moscardini L., 2012, MNRAS, 427, 3134

Boldrin M., Giocoli C., Meneghetti M., Moscardini L., Tormen G., Biviano A., 2016, MNRAS, 457, 2738

Bonamigo M., Despali G., Limousin M., Angulo R., Giocoli C., Soucail G., 2015, MNRAS, 449, 3171

Bosma A., 1981a, AJ, 86, 1791

Bosma A., 1981b, AJ, 86, 1825

Brax P. H., Martin J., 1999, Physics Letters B, 468, 40

Cooray A., Sheth R., 2002, Physics Reports, 372, 1

Cui W., Baldi M., Borgani S., 2012, MNRAS, 424, 993

Despali G., Giocoli C., Angulo R. E., Tormen G., Sheth R. K., Baso G., Moscardini L., 2016, MNRAS, 456, 2486

Despali G., Giocoli C., Bonamigo M., Limousin M., Tormen G., 2017, MNRAS, 466, 181

Despali G., Giocoli C., Tormen G., 2014, MNRAS, 443, 3208

Dolag K., Bartelmann M., Perrotta F., Baccigalupi C., Moscardini L., Meneghetti M., Tormen G., 2004, A&A, 416, 853

Fu L., Semboloni E., Hoekstra H., Kilbinger M., van Waerbeke L., Tereno I., Mellier Y., Heymans C., Coupon J., Benabed K., Benjamin J., Bertin E., Doré O., Hudson M. J., Ilbert O., Maoli et al. 2008, A&A, 479, 9

Giocoli C., Di Meo S., Meneghetti M., Jullo E., de la Torre S., Moscardini L., Baldi M., Mazzotta P., Metcalf R. B., 2017, MNRAS, 470, 3574

Giocoli C., Jullo E., Metcalf R. B., de la Torre S., Yepes G., Prada F., Comparat J., Göttlober S., Kyplin A., Kneib J.-P., Petkova M., Shan H. Y., Tessore N., 2016, MNRAS, 461, 209

Giocoli C., Marulli F., Baldi M., Moscardini L., Metcalf R. B., 2013, MNRAS, 434, 2982

Giocoli C., Metcalf R. B., Baldi M., Meneghetti M., Moscardini L., Petkova M., 2015, MNRAS, 452, 2757

Giocoli C., Moreno J., Sheth R. K., Tormen G., 2007, MNRAS, 376, 977

Giocoli C., Tormen G., Sheth R. K., 2012b, MNRAS, 422, 185

Harnois-Déraps J., van Waerbeke L., 2015b, MNRAS, 450, 2857

Hildebrandt H., Viola M., Heymans C., Joudaki S., Kuijken K., Blake C., Erben T., Joachimi B., et al. 2017, MNRAS, 465, 1454

Hoekstra H., Bartelmann M., Dahle H., Israel H., Limousin M., Meneghetti M., 2013, Space Sci. Rev., 177, 75

Izard A., Fosalba P., Crocce M., 2018, MNRAS, 473, 3051

Jing Y. P., 2000, ApJ, 535, 30

Kaiser N., Squires G., 1993, ApJ, 404, 441

Kauffmann G., White S. D. M., 1993, MNRAS, 261, 921

Kilbinger M., 2014, ArXiv e-prints

Kilbinger M., Fu L., Heymans C., Simpson F., Benjamin J., Erben T., Harnois-Déraps J., Hoekstra H., Hildebrandt H., et al. 2013, MNRAS, 430, 2200

Kitching T. D., Heavens A. F., Alsing J., Erben T., Heymans C., Hildebrandt H., Hoekstra H., et al. 2014, MNRAS, 442, 1326

Kitching T. D., Taylor A. N., Cropper M., Hoekstra H., Hood R. K. E., Massey R., Niemi S., 2016, MNRAS, 455, 3319

Köhlinger F., Viola M., Valkenburg W., Joachimi B., Hoekstra H., Kuijken K., 2016, Mon. Not. Roy. Astron. Soc., 456, 1508

Lacey C., Cole S., 1993, MNRAS, 262, 627

Lacey C., Cole S., 1994, MNRAS, 271, 676

Laureijs R., Amiaux J., Arduini S., Augueres J. ., Brinchmann J., Cole R., Cropper M., Dabin C., Duvet L., et al. 2011, eprint arXiv: 1110.3193

Limousin M., Richard J., Jullo E., Jauzac M., Ebeling H., Bonamigo M., Alavi A., Clément B., Giocoli C., Kneib J.-P., Verdugo T., Natarajan P., Siana B., Atek H., Rexroth M., 2016, A&A, 588, A99

Lin C.-A., Kilbinger M., 2015a, A&A, 576, A24

Lin C.-A., Kilbinger M., 2015b, A&A, 583, A70

LSST Science Collaboration Abell P. A., Allison J., Anderson S. F., Andrew J. R., Angel J. R. P., Armus L., Arnett D., Asztalos S. J., Axelrod T. S., et al. 2009, eprint arXiv: 0912.0201

Lucchin F., Matarrese S., 1985, Phys. Rev. D, 32, 1316

Martinet N., Schneider P., Hildebrandt H., Shan H., Asgari M., Dietrich J. P., Harnois-Déraps J., Erben T., Grado A., Heymans C., Hoekstra H., Klaes D., Kuijken K., Merten J., Nakajima R., 2017, ArXiv e-prints

Maturi M., Angrick C., Pace F., Bartelmann M., 2010, A&A, 519, A23

Maturi M., Fedeli C., Moscardini L., 2011, MNRAS, 416, 2527

Meneghetti M., Bartelmann M., Dahle H., Limousin M., 2013, Space Sci. Rev.

Meneghetti M., Melchior P., Grazian A., De Lucia G., Dolag K., Bartelmann M., Heymans C., Moscardini L., Radovich M., 2008, A&A, 482, 403

Metcalf R. B., Petkova M., 2014, MNRAS, 445, 1942

Monaco P., 2016, Galaxies, 4, 53

Monaco P., Sefusatti E., Borgani S., Crocce M., Fosalba P., Sheth R. K., Theuns T., 2013, MNRAS, 433, 2389

Munari E., Monaco P., Sefusatti E., Castorina E., Mohammad F. G., Anselmi S., Borgani S., 2017, MNRAS, 465, 4658

Navarro J. F., Frenk C. S., White S. D. M., 1996, ApJ, 462, 563

Neto A. F., Gao L., Bett P., Cole S., Navarro J. F., Frenk C. S., White S. D. M., Springel V., Jenkins A., 2007, MNRAS, 381, 1450

Perlmutter S., Aldering G., Goldhaber G., Knop R. A., Nugent P., Castro P. G., Deustua S., et al. 1999, ApJ, 517, 565

Petkova M., Metcalf R. B., Giocoli C., 2014, MNRAS, 445, 1954

Pires S., Leonard A., Starck J.-L., 2012, MNRAS, 423, 983

Planck Collaboration Ade P. A. R., Aghanim N., Arnaud M., Ashdown M., Aumont J., Baccigalupi C., Banday A. J., Barreiro R. B., Bartlett J. G., et al. 2016, A&A, 594, A24

Postman M., Coe D., Benítez N., Bradley L., Broadhurst T., Donahue M., Ford H., Graur et al. 2012, ApJS, 199, 25

Radovich M., Formicola I., Meneghetti M., Bartalucci I., Bourdin H., Mazzotta P., Moscardini L., Ettori S., Arnaud M., Pratt G. W., Aghanim N., Dahle H., Douspis M., Pointecouteau E., Grado A., 2015, A&A, 579, A7

Rasia E., Meneghetti M., Martino R., Borgani S., Bonafede A., Dolag K., Ettori S., Fabjan D., Giocoli C., Mazzotta P.,

Merten J., Radovich M., Tornatore L., 2012, New Journal of Physics, 14, 055018
Reischke R., Maturi M., Bartelmann M., 2016, MNRAS, 456, 641
Riess A. G., Filippenko A. V., Challis P., Clocchiatti A., Diercks A., Garnavich P. M., Gilliland R. L., et al. 1998, AJ, 116, 1009
Riess A. G., Strolger L., Casertano S., Ferguson H. C., Mobasher B., Gold B., Challis P. J., Filippenko A. V., Jha S., Li W., et al. 2007, ApJ, 659, 98
Riess A. G., Strolger L.-G., Tonry J., Casertano S., Ferguson H. C., Mobasher B., Challis P., Filippenko A. V., et al. 2004, ApJ, 607, 665
Rubin V. C., Burstein D., Ford Jr. W. K., Thonnard N., 1985, ApJ, 289, 81
Rubin V. C., Ford Jr. W. K., Thonnard N., 1980, ApJ, 238, 471
Schrabback T., Hartlap J., Joachimi B., Kilbinger M., Simon P., Benabed K., Bradač M., Eifler T., Erben et al. 2010, A&A, 516, A63+
Seitz C., Schneider P., 1995, A&A, 297, 287
Shan H., Liu X., Hildebrandt H., Pan C., Martinet N., Fan Z., Schneider P., Asgari M., et al. 2017, ArXiv e-prints
Sheth R. K., Tormen G., 2004, MNRAS, 350, 1385
Springel V., 2005, MNRAS, 364, 1105
Springel V., White S. D. M., Jenkins A., Frenk C. S., Yoshida N., Gao L., Navarro J., Thacker R., Croton D., Helly J., Peacock J. A., Cole S., Thomas P., Couchman H., Evrard A., Colberg J., Pearce F., 2005, Nature, 435, 629
Springel V., White S. D. M., Tormen G., Kauffmann G., 2001b, MNRAS, 328, 726
Tinker J., Kravtsov A. V., Klypin A., Abazajian K., Warren M., Yepes G., Gottlöber S., Holz D. E., 2008, ApJ, 688, 709
Tormen G., 1998, MNRAS, 297, 648
van den Bosch F. C., 2002, MNRAS, 331, 98
Wechsler R. H., Bullock J. S., Primack J. R., Kravtsov A. V., Dekel A., 2002, ApJ, 568, 52
Wechsler R. H., Zentner A. R., Bullock J. S., Kravtsov A. V., Allgood B., 2006, ApJ, 652, 71
Wetterich C., 1988, Nuclear Physics B, 302, 668
White S. D. M., Rees M. J., 1978, MNRAS, 183, 341
White S. D. M., Silk J., 1979, ApJ, 231, 1
Zhao D. H., Jing Y. P., Mo H. J., Bnörner G., 2009, ApJ, 707, 354
Zorrilla Matilla J. M., Haiman Z., Hsu D., Gupta A., Petri A., 2016, Phys. Rev. D, 94, 083506
Zwicky F., 1937, ApJ, 86, 217